

Smoothed particle hydrodynamics simulations of flow separation at bends



Q. Hou^{a,*}, A.C.H. Kruisbrink^b, F.R. Pearce^c, A.S. Tijsseling^d, T. Yue^c

^aState Key Laboratory of Hydraulic Engineering Simulation and Safety, School of Civil Engineering, Tianjin University, Tianjin, China

^bSchool of Mechanical, Materials and Manufacturing Engineering, The University of Nottingham, Nottingham, UK

^cSchool of Physics and Astronomy, The University of Nottingham, Nottingham, UK

^dDepartment of Mathematics and Computer Science, Eindhoven University of Technology, Eindhoven, The Netherlands

ARTICLE INFO

Article history:

Received 2 January 2013

Received in revised form 5 August 2013

Accepted 15 November 2013

Available online 1 December 2013

Keywords:

SPH

Flow separation

Channel bend

Free streamline

Flow contraction coefficient

ABSTRACT

The separated flow in two-dimensional bends is numerically simulated for a right-angled bend with different ratios of the channel widths and for a symmetric bend with different turning angles. Unlike the potential flow solutions that have several restrictive assumptions, the Euler equations are directly solved herein by the smoothed particle hydrodynamics (SPH) method, which is a Lagrangian approach without a mesh. The coefficient of flow contraction is obtained in terms of the ratio of the channel widths and the turning angle. The velocity field and pressure distribution in a right-angled bend are calculated. The shape of the free streamlines for a symmetric bend with several turning angles is obtained. The numerical steady-state results are validated against available theoretical solutions. The computed velocity on the free streamline is consistent with Kirchhoff's theory.

© 2013 Elsevier Ltd. All rights reserved.

1. Introduction

Flow separation occurring in piping systems has received much attention because it determines the energy losses, pressure coefficients, flow contraction coefficients and forces on components such as pipes, valves, tees and bends. When a fluid passes a bend, it is likely to separate from the inner corner (see Fig. 1). The size of the separation void depends on the Reynolds number of the flow and the geometry of the bend. To model the flow separation problem, there are two possible ways to go. One is to use potential flow theory and the other is to solve numerically the full Navier–Stokes equations. Although the energy losses resulting from separation cannot be directly predicted by potential flow theory, a good estimate of the size of the separation region, the velocity gradients and the pressure distribution can be obtained. The potential flow solution usually agrees well with that of a high Reynolds flow. One can predict the energy dissipation resulting from flow separation through solving the Navier–Stokes equations. Such solutions can be quite difficult to obtain because of turbulence and because the separation streamline is not known in advance. Therefore, only potential flow theory applied to flow separation in bends is considered herein and briefly reviewed below.

Using conformal mapping and Roshko's free-streamline theory [1], Lichtarowicz and Markland [2] solved the potential flow round a right-angled elbow for two different ratios of the channel widths $R_b := s/b$ (see Fig. 1). In Roshko's model, separation is introduced through a free streamline that divides the flow in the bend into two regions: (1) the main flow where the velocity is continuous and possesses a potential, and (2) a secondary region extending theoretically to infinity. The separated free streamline is assumed to start from point C, curve gradually until its direction is that of the secondary flow and then remain straight and parallel to the wall. The position of the juncture point E and the velocity along the streamline V_s are functions of the ratio of the velocity at the separation point to the velocity far downstream. By mapping the physical plane onto a hodograph domain, Mankbadi and Zaki [3] studied the flow patterns in symmetric and asymmetric bends with various turning angles β (see Fig. 2). In contrast to Lichtarowicz and Markland [2], Kirchhoff's free-streamline theory has been used in [3]. In Kirchhoff's theory, the curved free streamline starts from point C and asymptotically extends to infinity. That is, there is no second flow region as in Roshko's model. The velocity on the free streamline CE' is assumed to remain constant and is equal to that of the downstream flow, i.e. $V_s = V_d$. The hodograph transformation method used in [3,4] is efficient for two-dimensional and axisymmetric problems [4,5]. According to Hassenpflug [6], when the liquid is at very high Reynolds numbers and the region adjacent to the free streamline is gas, the model is a good

* Corresponding author. Address: School of Computer Science and Technology, Tianjin University, Tianjin 300072, China. Tel.: +86 22 27402339.

E-mail address: darcy.hou@gmail.com (Q. Hou).

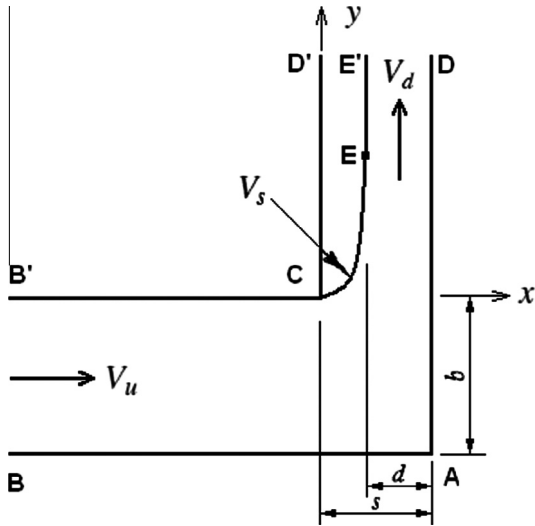


Fig. 1. Definition sketch of separated flow in a right-angled bend.

description of the actual physical flow. However, the solution procedure of the indirect hodograph method is rather restrictive [4], and in practice it is difficult to impose the boundary conditions as assumed in the theory [6].

During the early developments (1980s) of the smoothed particle hydrodynamics (SPH) method, it was mainly applied to compressible astrophysical flows [7]. Today SPH is used to model the collapse and formulation of galaxies, coalescence of black holes with neutron stars, detonations in white dwarfs and even the evolution of the universe [8,9]. At the beginning of the 1990s, SPH was extended to model high velocity impact problems of solids [10] and incompressible free-surface flows [11]. Now SPH is used to simulate a vast range of fluid dynamic problems as shown in the recent reviews [12,13]. However, there is not much published work on SPH applications to pipe related flows, which are generally treated as 1D problems. For 1D flows, SPH has less advantage over traditional mesh-based methods than for 2D and 3D flows. The most studied case is the shock tube problem [7,8,14]. Lastiwka et al. [15] used SPH for 1D compressible nozzle flows. Recently, it was

successfully employed to model rapid pipe filling [16], water hammer [17] and slug impact [18]. The SPH simulations of the 2D impinging jet on an inclined wall [19–21] have close relationship with the problem considered herein.

The SPH method is applied in this paper to study flow separation at bends with various aspect ratios R_b (Fig. 1) and turning angles β (Fig. 2). The SPH approximations discretize the spatial derivatives through particles that move with the flow. The flow properties carried by the moving particles are computed from interaction with their neighboring particles. A priori connectivity between the particles is not required. As free surfaces are naturally captured and represented by moving particles, the dedicated surface tracking techniques encountered in traditional mesh-based methods are not needed.

The paper is organized as follows. Section 2 presents the discrete SPH equations describing inviscid flow. The numerical treatment of various boundary conditions is described and several important aspects of the numerical implementation are discussed. In Section 3, the obtained numerical results are compared with theoretical results. Concluding remarks are given in Section 4.

2. SPH fluid dynamics

The SPH equations describe the evolution of the flow and the motion of material points that are referred to as particles. Each particle, e.g. particle labeled a , carries a constant mass m_a , and a time-dependent density ρ_a , pressure p_a and velocity \mathbf{v}_a . The particle changes its position \mathbf{r}_a according to the flow velocity. In contrast to traditional Eulerian methods, SPH is a Lagrangian particle solver where the particle connectivity evolves with time and needs to be determined by a particle search. The SPH equations for a compressible gas are described in [7]. Herein the SPH equations for a weakly compressible inviscid fluid are presented. More details can be found in the recent review [13].

2.1. Discrete SPH equations

The definition sketches of a separated flow inside a right-angled bend and a symmetric bend with an arbitrary turning angle β are shown in Figs. 1 and 2, respectively. The fluid flows in the bend from the inlet BB' to the outlet DD' . Two outer walls BA and AD , and two inner walls $B'C$ and CD' , form the fixed boundaries. At point C the flow separates from the wall and follows the curved free streamline CE' . The flow is assumed to be two-dimensional and the modeled fluid is weakly compressible and inviscid. There is no gravity, so that Figs. 1 and 2 are top views. The problem is governed by the Euler equations, which in discrete SPH form read [11,13]:

$$\frac{D\rho_a}{Dt} = \sum_b m_b \mathbf{v}_{ab} \cdot \nabla_a W_{ab}, \quad (1)$$

$$\frac{D\mathbf{v}_a}{Dt} = -\sum_b m_b \left(\frac{p_a}{\rho_a^2} + \frac{p_b}{\rho_b^2} + \Pi_{ab} \right) \nabla_a W_{ab}. \quad (2)$$

In the discrete SPH continuity Eq. (1), subscripts a and b denote a reference particle a and its neighbors b ; $\mathbf{v}_{ab} := \mathbf{v}_a - \mathbf{v}_b$; $W_{ab} := W(\mathbf{r}_a - \mathbf{r}_b, h)$ is the kernel (see Section 2.3); $\nabla_a W_{ab}$ is the gradient of the kernel taken with respect to the position of particle a . The smoothing length h is a size scale of the kernel support and determines the degree that a particle interacts with its neighbors. In the discrete SPH momentum Eq. (2), Π_{ab} is an artificial viscous term that has the general form

$$\Pi_{ab} := \frac{-\alpha c_0 h}{\bar{\rho}_{ab}(r_{ab}^2 + 0.01h^2)} \min(\mathbf{v}_{ab} \cdot \mathbf{r}_{ab}, 0), \quad (3)$$

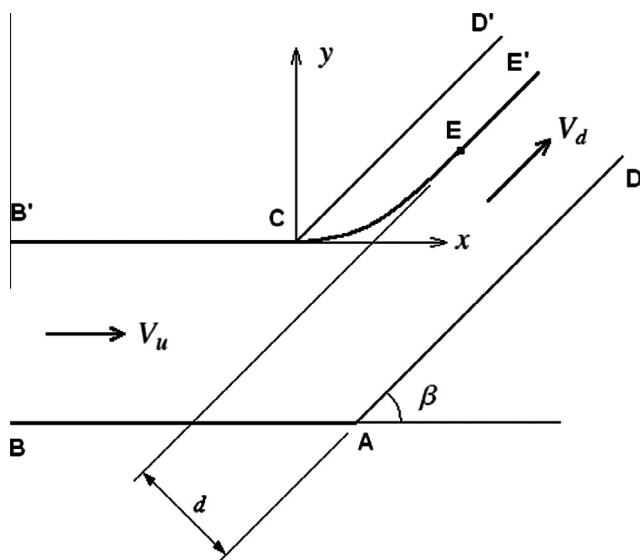


Fig. 2. Definition sketch of separated flow in a symmetric bend with turning angle β .

in which c_0 is the speed of sound, $\mathbf{r}_{ab} := \mathbf{r}_a - \mathbf{r}_b$, $r_{ab} := |\mathbf{r}_{ab}|$, $\rho_{ab} := (\rho_a + \rho_b)/2$, and α is a problem-dependent constant [7,11]. Here we take $\alpha = 0.1$ as proposed in [20] for free-surface flows. This artificial term produces a shear and bulk viscosity in the flow.

To close the system, the gauge pressure of particle a correlates to its density by an equation of state [22],

$$p_a = c_0^2(\rho_a - \rho_0), \quad (4)$$

where ρ_0 is the fluid density at a reference pressure. The value of c_0 needs some care as explained below. For hydraulic and acoustic pressure variations, the relative density variation $\delta\rho/\rho$ is proportional to Ma^2 [11] and Ma , respectively, where $\text{Ma} := V/c_0$ is the Mach number and V is a typical convective velocity. Since V is generally two or three orders of magnitude smaller than c_0 , $\delta\rho/\rho$ is extremely small. In SPH, incompressible and weakly compressible fluids are approximated by an artificial fluid which is much more compressible. The relative density variation $\delta\rho/\rho$ is generally taken to be about 1% by using an artificial speed of sound c_0 . After the estimation of a typical velocity V , e.g. the inflow velocity in this study, a suitable choice of c_0 produces the desired density variation of about 1%.

2.2. Boundary conditions

For the problems considered herein, four types of boundary conditions need to be numerically treated. They are the free-slip wall, free surface, inlet and outlet. The mathematical statements of these boundary conditions can be found in e.g. [21,23]. Here we briefly discuss their treatment in SPH; further details can be found in [21].

There are several methods to deal with the free-slip wall condition. The wall particle method [11] is easy to implement and useful for irregular boundaries. It used to be popular but is rarely used now, because non-physical shear stresses may occur. The fixed ghost particle method proposed by Morris et al. [22] is another choice. It was mainly used for no-slip boundary conditions, and its recent extension to free-slip walls using interpolation and extrapolation techniques is detailed in [24]. Based on an idea similar to the fixed ghost particle method, Adami et al. [25] recently proposed a new approach. Another common way to enforce the free-slip condition is to use a local mirroring of the fluid particles onto the other side of the solid boundary [26,27]. At each time step an image of the flow is generated. The thickness of the mirror particle layer is slightly larger than the kernel radius to ensure that all kernels are complete. To exactly satisfy the free-slip condition, the tangent velocity is the same as that of the fluid particle, whilst the normal velocity is in opposite direction [21]. The mirror particle approach is used in this study; its efficiency has been underlined by Monaghan [13].

As seen in Figs. 1 and 2, when two straight walls join at some point, a corner (geometric singularity) is formed. To complete the support of the kernel associated with particles close to the corner, additional treatment is needed. For consistency, a similar idea as the mirror particle approach is applied. The empty space which is left behind the two walls is filled with corner mirror particles by applying a point-symmetry to the fluid particles near the corner. The treatment of geometric singularities with the fixed ghost particle method is described in [24].

On the free surface two conditions need to be satisfied. The kinematic condition implies that a particle originally on the surface will remain on it. This is naturally satisfied by the Lagrangian particle movement. The dynamic condition ($p = 0$) is automatically satisfied too due to the SPH formulation of the continuity equation and spatial derivative [21,28]. The automatic enforcement of the

free surface conditions is an inherent advantage of SPH over traditional mesh-based methods.

The boundary conditions at the inlet and outlet are enforced by using the image particle approach [15,20,29]. An inflow buffer block is placed ahead of the planar inlet boundary. The thickness of the block is $2.5h$, which is slightly larger than the support radius of the kernel. In the inlet block, there are predefined image particles (referred to as inlet particles). An inlet particle moves with its given velocity. After crossing the inlet and entering the fluid domain, it becomes a fluid particle and the flow field associated with it will evolve from the next step on. A new inlet particle is created at the upstream end of the inlet buffer block. Similarly, an outflow buffer block is placed behind the outlet boundary to ensure that the fluid flows out of the fluid domain freely. When a fluid particle leaves the fluid domain and enters the outlet block, it becomes an outlet particle whose properties will not change. It will be deleted after leaving the outflow buffer block at its downstream end. This is different from the non-reflecting SPH boundary proposed by Lastiwka et al. [15], in which an extrapolation is necessary to calculate the flow fields in the buffer blocks. The inflow and outflow sections should be far enough from the bend to avoid any influence from the creation of inlet and removal of outlet particles [21].

2.3. Kernel and its gradient

The use of different kernels W_{ab} with different h is the SPH analogue of using different stencils in finite-difference methods [30]. Fulk and Quinn [31] analyzed 20 different SPH kernels and concluded that the bell-shaped kernels usually perform better than other shapes. The following bell-shaped cubic-spline kernel has been proven to be computationally accurate [7,31]:

$$W(q) := G \begin{cases} 1 - 1.5q^2 + 0.75q^3, & 0 \leq q < 1, \\ 0.25(2 - q)^3, & 1 \leq q < 2, \\ 0, & q \geq 2, \end{cases} \quad (5)$$

where $q := r_{ab}/h$ and the normalizing coefficient G is $10/(7h\pi)$ for two-dimensional problems. The cubic-spline kernel and its derivatives are shown in Fig. 3.

For free-surface flows, the smoothing length is generally taken as $h = \eta d_0$ where $\eta = 1.1-1.33$ [11,20,32] and d_0 is the initial particle spacing (particles are placed on a square lattice). Here we take $\eta = 1.33$ as in [20]. To avoid possible ‘‘pairing instability’’ resulting from a relatively large η [14], the ‘‘hum’’ in the kernel gradient is

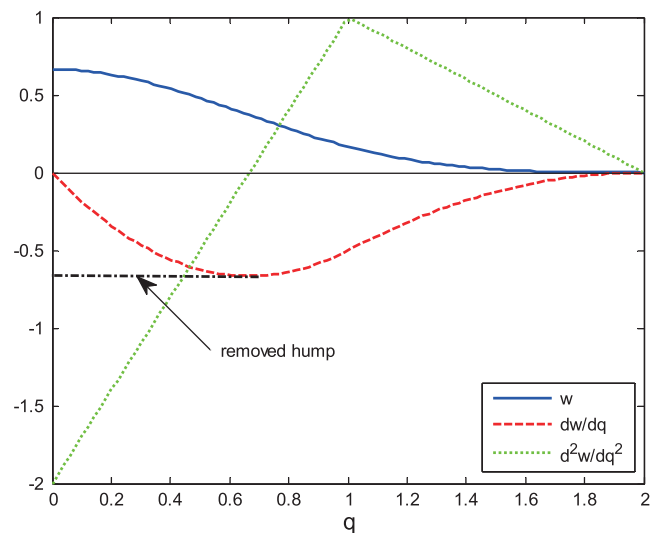


Fig. 3. The cubic spline kernel $W(q)$ and its derivatives.

removed by simply making the kernel gradient constant for $q < 2/3$ [33] (see Fig. 3). As discussed by Price [14], “Whilst removing the hump cures the pairing instability, one should be careful about employing such a gradient in practice since the kernel gradient is no longer exactly normalized. The pairing instability is the main reason one cannot simply stretch the cubic spline to large neighbor numbers in order to obtain convergence.”

2.4. Time stepping

Starting from an initial distribution (\mathbf{r}_a) of particles with given mass m_a (constant in time), densities ρ_a and velocities \mathbf{v}_a , the basic Eqs. (1), (2) are solved at each time step for each particle. For time integration Euler’s forward method is used herein, which is first-order accurate, fully explicit, and conditionally stable. A recommended time step size satisfying the Courant-Friedrichs-Lewy (CFL) criterion is [22]:

$$\Delta t \leq C_{CFL} \frac{h}{c_0 + |V|}, \tag{6}$$

where C_{CFL} is a constant between 0 and 1. With $Ma = |V|/c_0$ the CFL condition (6) can be rewritten as

$$\Delta t \leq C \frac{d_0}{c_0}, \tag{7}$$

where the constant $C = \eta C_{CFL}/(1 + Ma)$ is taken as 0.2 herein. In addition, a time-step constraint related to acceleration has to be satisfied by [34]:

$$\Delta t \leq \frac{1}{4} \min_b \left(\sqrt{\frac{h}{|\mathbf{a}|_b}} \right), \tag{8}$$

where $|\mathbf{a}|_b = |D\mathbf{v}_b/Dt|$ is the magnitude of particle acceleration and the minimum is over all particles.

To efficiently find and access neighboring particles at each time step, the link-list algorithm with an optimized cell size [35] is used.

3. Numerical results

Two series of flow separation problems in rectangular channels are simulated. The right-angled elbow shown in Fig. 1 is considered first. The width of the upstream channel is fixed at $b = 1$ m, whilst the downstream channel width s is varied and related to b by the ratio of channel widths R_b . The length of the inner walls B/C and CD' is 2 m. The length of the outer wall AD is 3 m and the length of BA depends on the given value of R_b . The second series of simulations concern flow separation at a symmetric bend ($R_b = 1$) with various turning angles β (see Fig. 2). The lengths of B/C and CD' and the channel width b are the same as above. The chosen lengths of the outer walls depend on the given turning angle β .

In the SPH setup, there are uniformly distributed fluid particles upstream of the bend ($X < 0$) and inlet particles in the inflow section with particle spacing $d_0 = 0.05$ m ($b/d_0 = 20$). The pressure is zero and the velocity components are $V_u = V_x = 1$ m/s and $V_y = 0$. The artificial speed of sound is taken as $c_0 = 15$ m/s, which gives a sufficiently low Mach number. The time step for all cases considered herein is fixed at 0.0001 s, which is small enough to satisfy the stability conditions (7) and (8). When the kinetic energy of all particles in the computational domain becomes constant (relative difference between two time steps is less than a given tolerance), the simulation is stopped and assumed to have reached its steady state. The spatial coordinates are scaled by the upstream channel width: $X = x/b$ and $Y = y/b$.

For a right-angled elbow with $R_b = 1$, the SPH solution is shown in Fig. 4, where the outer particle layer represents the free streamline. The solutions from potential flow theory are also presented

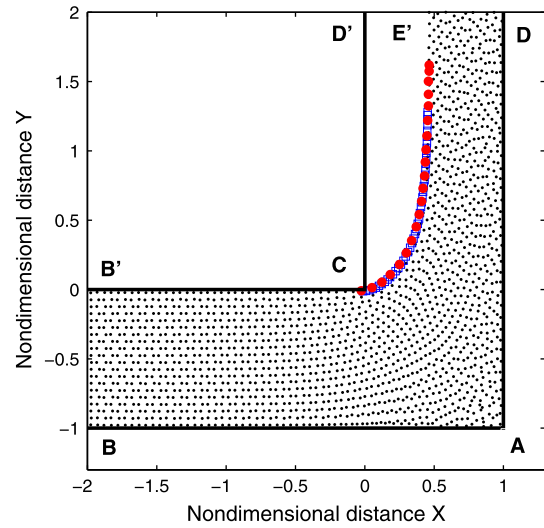


Fig. 4. Particle paths and theoretical free-streamline in a right-angled bend. Dots – SPH particles; open squares – L&M [2]; filled circles – Chu [4].

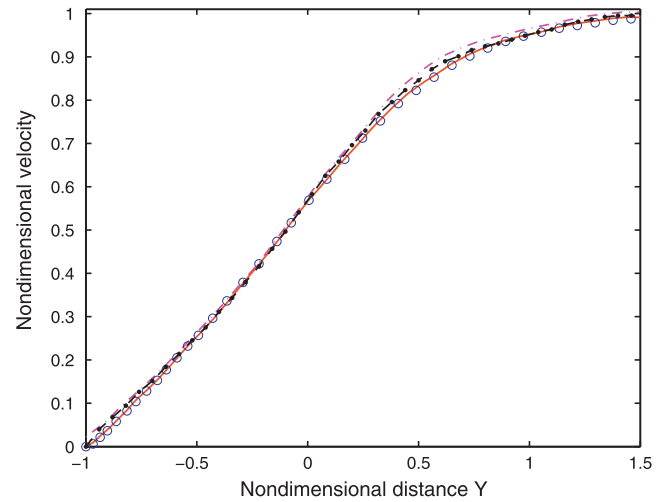


Fig. 5. Velocity distribution along wall AD . Dashed line – SPH with $b/d_0 = 10$, solid line with dots – SPH with $b/d_0 = 20$, solid line – SPH with $b/d_0 = 40$; open circles – Chu [4].

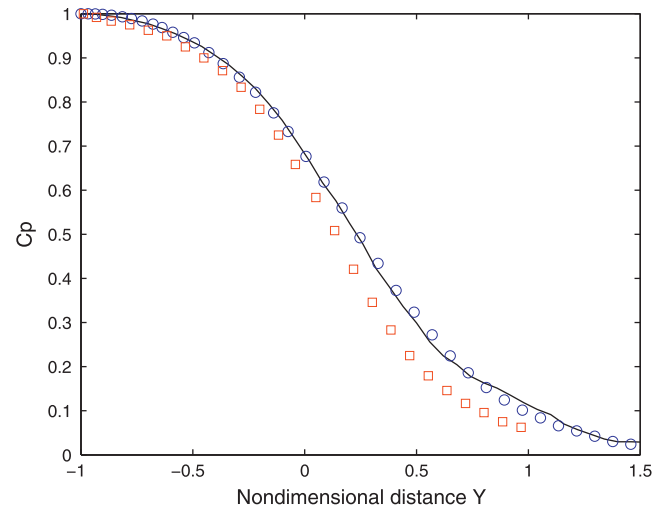


Fig. 6. Non-dimensional pressure along wall AD . Solid line – present SPH; open squares – L&M [2]; open circles – M&Z [3].

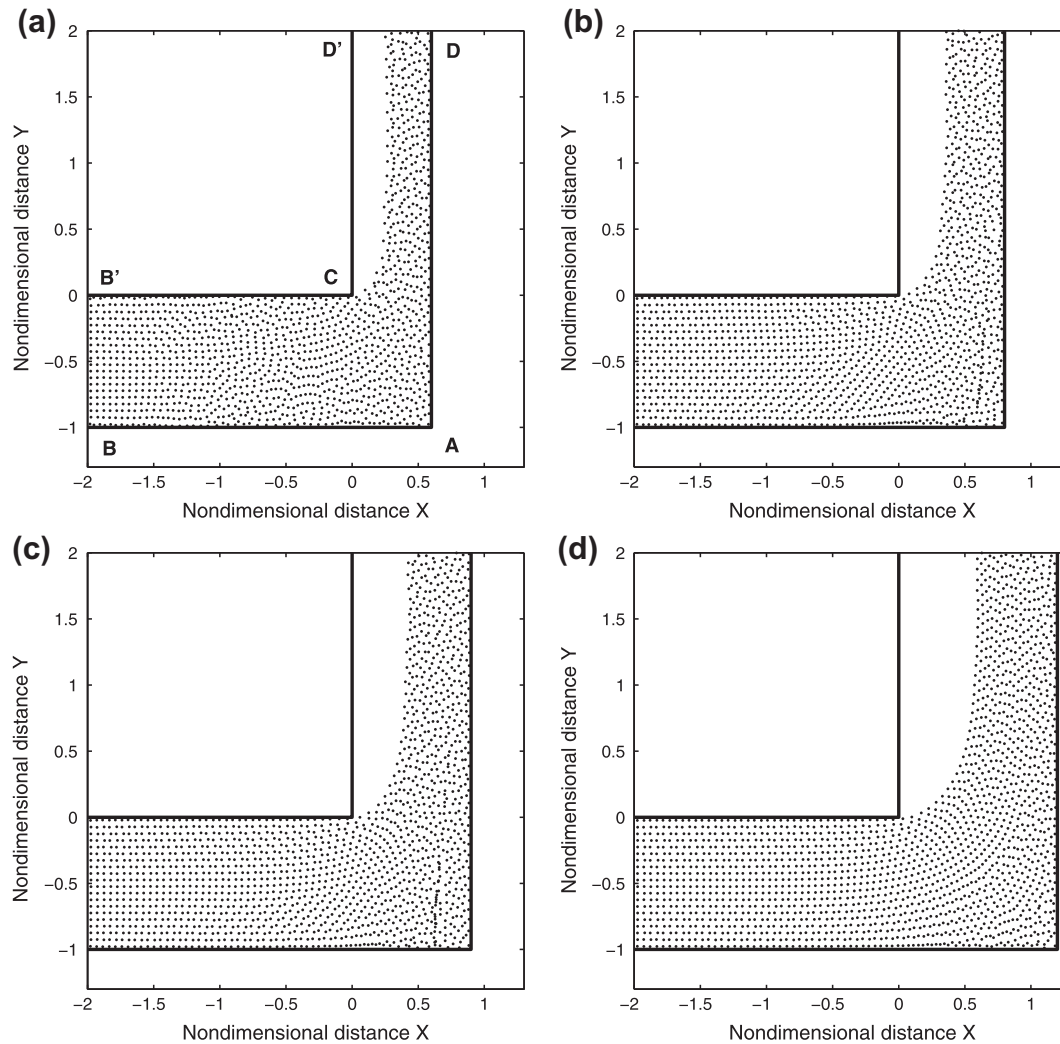


Fig. 7. Flow in a right-angled bend for different ratios of channel widths: (a) $R_b = 0.6$, (b) $R_b = 0.8$, (c) $R_b = 0.9$ and (d) $R_b = 1.2$.

Table 1

Values of contraction coefficients C_c for different ratios of channel widths R_b .

R_b (ratio)	0	0.5	0.6	0.7	0.8	0.9	1.0	1.2	1.3	1.5	2.0	∞
L&M [2]	0.611 ^c	0.584	0.573	0.560	0.551	0.537	0.526	0.500	– ^a	– ^a	– ^a	1.0 ^b
Present	– ^a	0.59	0.58	0.56	0.55	0.53	0.53	0.50	0.63	0.69	0.81	– ^a

^a No solution available.

^b Analytical solution given in [20,39].

^c Analytical solution given in [2].

for comparison. The computed free-streamline matches the theoretical solutions very well. The agreement of the current results with the solution of Lichtarowicz and Markland [2] is slightly better than with that of Chu [4]. Some error may be present in the results extracted from Chu [4], as his coordinate information is incomplete. The cross-sectional averaged outlet velocity at $Y = 2$ is $V_d = 1.89$ m/s, which is slightly smaller than the prediction ($V_d = 1.90$ m/s) of Chu [4]. The slip velocity distribution along wall AD , scaled by V_d , is shown in Fig. 5. The SPH prediction is consistent with the theoretical solution of [4]. The particle velocity along the free streamline CE is constant at a value close to the averaged outlet velocity V_d . This is consistent with Kirchhoff's free-streamline theory.

To show the numerical convergence, simulations with coarser ($b/d_0 = 10$) and finer ($b/d_0 = 40$) initial particle spacings were per-

formed and the results are also presented in Fig. 5. The convergence is evident and the result with the highest resolution ($b/d_0 = 40$) has the best agreement with the theory. The convergence rate is of first order [21], which is consistent with the results of other researchers [36–38]. Since the SPH solution with $b/d_0 = 20$ is sufficiently accurate for illustration purposes, the following results are obtained with this particle resolution.

The distribution of the pressure coefficient C_p is shown in Fig. 6, together with the results of Lichtarowicz and Markland [2] and Mankbadi and Zaki [3]. The pressure coefficient is defined as $C_p := p/(\rho V_d^2/2)$, in which p is the pressure along the outer wall AD . There are two ways to determine the SPH pressure p at steady state. One way is to derive it from the velocity distribution through the Bernoulli theorem, which is entirely consistent with the steady Euler equations. In this approach, the velocity along the wall is cal-

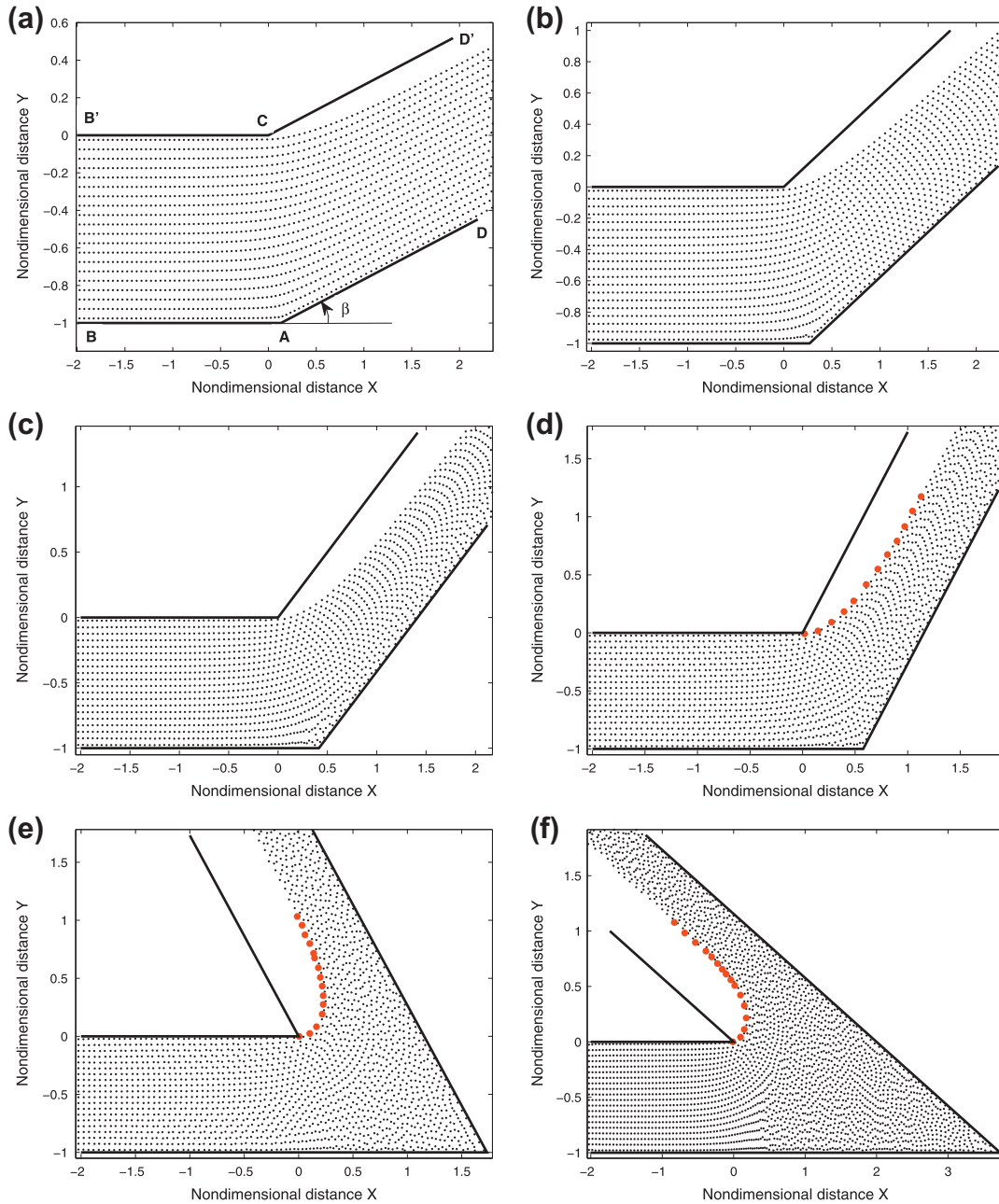


Fig. 8. Flow in symmetric bends with various turning angles: (a) $\beta = 15^\circ$, (b) $\beta = 30^\circ$, (c) $\beta = 45^\circ$, (d) $\beta = 60^\circ$, (e) $\beta = 120^\circ$ and (f) $\beta = 150^\circ$. Dots – SPH particles; Filled circles – Chu [4].

Table 2
Values of contraction coefficients C_c for different turning angles β .

β ($^\circ$)	15	30	45	60	90	120	150
Chu [4]	0.893	0.792	0.701	0.625	0.528	0.467	0.434
Present	0.89	0.79	0.70	0.63	0.53	0.47	0.43

culated first by interpolating the particle velocities as shown in Fig. 5. The pressure is then computed according to the Bernoulli equation. The other way is to directly interpolate from the particles describing the pressure field. The SPH results shown in Fig. 6 are determined by the first approach. The predicted C_p by SPH has better agreement with the solutions of Lichtarowicz and Markland [2] than with those of Mankbadi and Zaki [3]. This is consistent with the conclusion of Chu [4], that numerical errors may have been

present in the method of the latter. The directly interpolated pressure distribution (not shown here) has less satisfying agreement with the theoretical solutions because of noise in the pressure field [20,34].

For the asymmetric case ($R_b := s/b \neq 1$), four steady-state flow fields are displayed in Fig. 7. For the free streamlines, there are no theoretical results available for comparison, but the computed results can be verified to some extent through the contraction coefficient $C_c := d/b$ (see Fig. 1) as shown in Table 1. Note that the flow width DE' at the outflow section has a small variation in time due to particle fluctuations. Consequently, the evaluation of C_c involves averaging over a certain time interval at steady – but slightly fluctuating – state. The calculated contraction coefficients agree very well with the theoretical ones. The maximum relative error is less than 1.5 percent.

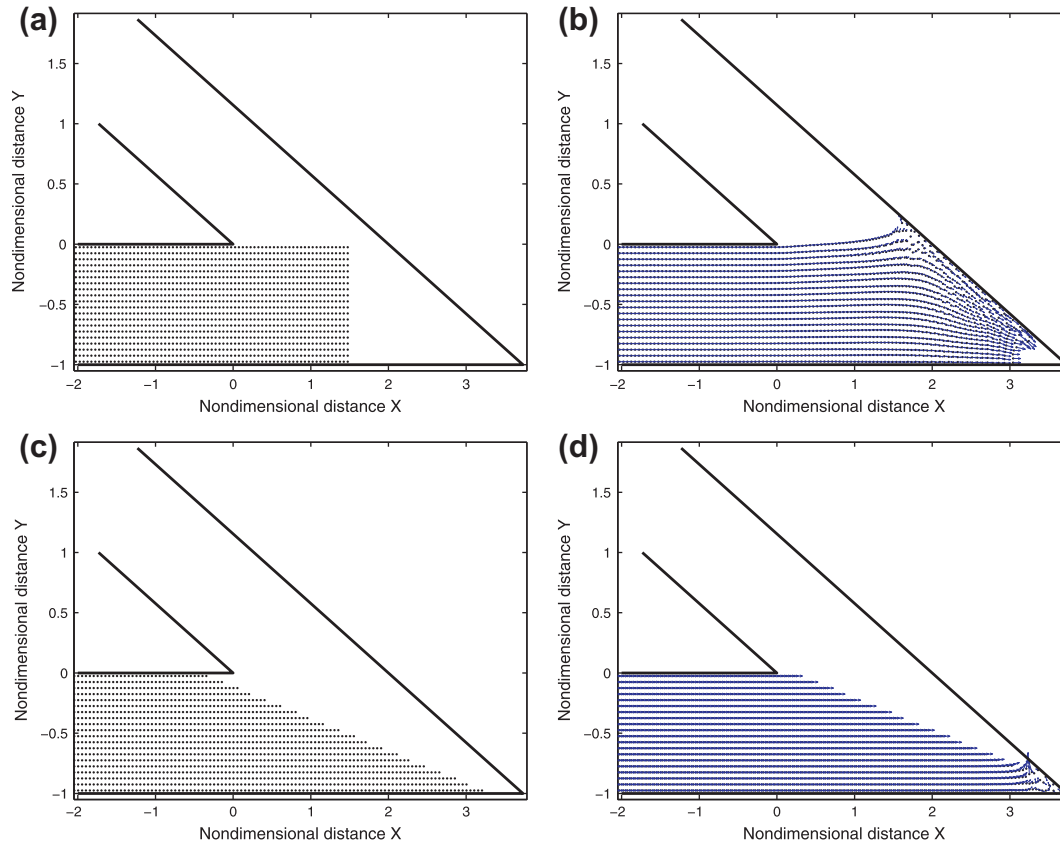


Fig. 9. Sketch of possible particle penetration at the outer corner when too small c_0 is used: (a) vertical front, (b) velocity distribution, (c) wedge front and (d) velocity distribution.

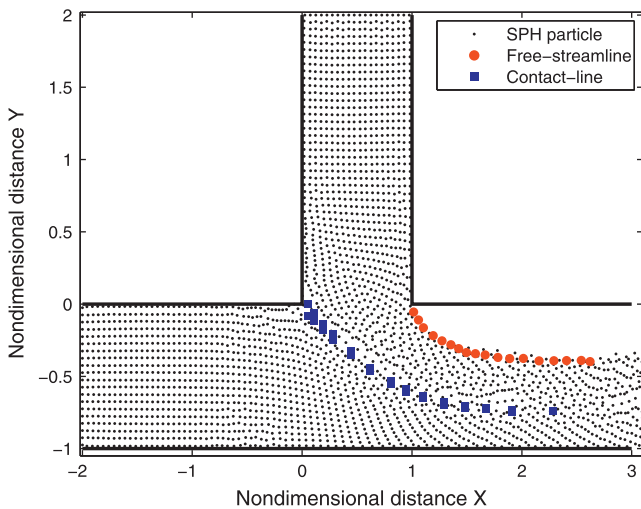


Fig. 10. Flow with free-streamline and contact-line in a channel with orthogonal side branch. Dots – SPH particles; Filled circles and squares – Hassenpflug [6].

As shown in Table 1, the contraction coefficient C_c decreases as R_b increases up to $R_b = 1.2$. When R_b becomes so large that the separation point C has no effect on the downstream flow, the current setup will be that of half of a jet emerging from a channel and impinging on an orthogonal plane [20,21]. That is, when R_b becomes large enough, the bend (i.e. outer wall AD) has no effect on the upstream parallel flow. Clearly, following the same definition, the contraction coefficient for that case is 1. That is, as $R_b \rightarrow \infty$ then $C_c \rightarrow 1$ [20,39]. As a consequence, there will be a

specific R_b (between 1.2 and 1.3) having a minimum value of C_c (about 0.5). On the other hand, when $R_b \rightarrow 0$, the contraction coefficient approaches another constant 0.611 [2]. This limit case cannot be simulated easily in the present method or any other mesh-based numerical method. In fact, when R_b equals 0.5, the simulated flow has become so violent that the effect of the inlet location is not negligible anymore.

Typical results of the second series of simulations ($R_b = 1$ with different angle β) are shown in Fig. 8 together with results from potential flow theory. For the first three cases $\beta = 15^\circ, 30^\circ$ and 45° , the theoretical curves of the free streamlines were not given in [3,4]. For the other three cases $\beta = 60^\circ, 120^\circ$ and 150° , the numerical results agree very well with the theoretical solutions. The contraction coefficients for various turning angles are shown in Table 2. The numerical results are consistent with the theoretical predictions. The relative error is less than 1 percent.

To reach the final steady state, the simulation time varied from 4 seconds ($\beta = 15^\circ$) to 5 seconds ($\beta = 150^\circ$). That is, after about 45,000 time-steps, the plotted final states were achieved. All the calculations were performed on a standard PC, and the computation time was between 15 and 25 minutes for one complete case. The number of fluid particles in steady state varied from 1800 ($\beta = 15^\circ$) to 2950 ($\beta = 150^\circ$). The obtained agreement can even be further improved by increasing b/d_0 (reducing the initial particle spacing d_0) at the expense of computational time. By halving the particle spacing, the number of fluid particles at steady state is approximately four times more, and hence the CPU time will increase four times. As shown in Fig. 8, with the increasing of β , a larger portion of the flow is affected by the outer corner of the bend, and less particles stay in smooth streamlines when rounding the bend. When the turning angle is larger than 90° , some fluid particles remain trapped at the outer corner (see Figs. 8e and 8f).

Based on Table 2, the estimated maximum velocity at steady state for the cases considered is $V_{\max} = V_u/C_c < 2.5$ m/s. Thus a speed of sound $c_0 = 25$ m/s should guarantee the SPH requirement of low Mach number for all test cases. However, when $c_0 = 25$ m/s is used, during the early unsteady stage, particles penetrate through the outer corner of bends with large turning angles (e.g. $\beta = 120^\circ$ and 150°). The reason is that the maximum velocity during the unsteady part of the numerical simulation can be much higher than 2.5 m/s. For a flow starting with a vertical front (see Fig. 9a), a large portion of it will turn downwards to the outer corner because there is no entrapped air to prevent it (see Figs. 2 and 9b). Due to conservation of volume, the local flow velocity increases and attains a high value before it arrives at the outer corner, e.g. a velocity of 9.5 m/s in the $\beta = 150^\circ$ case. The pressure forces exerted by mirror particles at the opposite side of the wall are not high enough to fully stop the high velocity particles going into the corner, and some particles penetrate through the geometric singularity. This artefact happens mainly during the early unsteady phase of the simulation, and fully disappears at steady state.

To avoid early-stage particle penetration, a possible way is to use a larger c_0 , i.e. $c_0 = 95$ m/s, to fulfill the requirement of low Mach number. This increases the pressure forces exerted by the mirror particles. However, when $c_0 = 95$ m/s is used, the Mach number at steady state will not be within the desired range $\Delta\rho/\rho = \text{Ma}^2 \sim 1\%$. Hence a time-dependent speed of sound should be used at the expense of one more equation that needs to be solved (see e.g. [40] for this new concept). In fact, there is a simpler way to avoid early-stage particle penetration without using a larger or time-dependent c_0 than practically desired. The initial flow is set up with a wedge front (the angle of which is larger than β) as shown in Fig. 9c. The maximum velocity during the early unsteady state is now reduced to 1.4 m/s and the particle distribution is less disordered (see Fig. 9d). Although the ultimate free-streamline profiles at steady state show no significant change, the unsteady simulation becomes smoother, and the steady state is achieved earlier.

Another practical situation is the flow in branched channels as systematically studied by Hassenpflug [6]. To demonstrate the capability of the present method to simulate flow separation in branched channels, the first example of Hassenpflug [6] consisting of two perpendicular inlets with identical flow velocities is examined here, and the results are shown in Fig. 10. To avoid double particle mirroring at the left inner corner, two orthogonal continuous walls [28] with a length of $2h$ were used for the enforcement of the free-slip condition. It is seen that for both the free streamline and the contact line of the two inflows, the computed solutions are consistent with the analytical solution. The small differences are mainly due to the current coarse particle distribution and can be diminished by using more particles.

4. Concluding remarks

The problem of flow separation at bends with various leg ratios and turning angles has numerically been simulated by the SPH particle method. The obtained steady states are compared to analytical solutions from potential flow theory. For a right-angled bend with different ratios (R_b) of downstream to upstream channel width, the computed free-streamline trajectories agree well with the theory. The difference between the calculated and theoretical flow contraction coefficients is small, with a 1.5 percent maximum relative error. As R_b increases, the contraction coefficient first decreases from 0.6 to a minimum value of 0.5 and then increases to a maximum value of 1. The corresponding limit case $R_b \rightarrow \infty$ corresponds to jet flow impinging on a perpendicular wall. For symmetric bends with various turning angles, the computed free

streamlines and contraction coefficients match the theoretical results with a maximum relative error of 1 percent. One example of flow merging in a branched channel has been simulated and good agreement with theory was found. The current SPH solver appears to be a powerful tool to deal with flow separation problems in channels. The steady solutions were in excellent agreement with theory; the unsteady solutions will be used to estimate impact forces on bends [18].

Acknowledgment

The first author is grateful to the China Scholarship Council (CSC) for financially supporting his PhD studies at Eindhoven University of Technology, The Netherlands. The support in part by the National Basic Research Program of China (No. 2013CB329301) and National Natural Science Foundation of China (No. 61233009) is highly appreciated too.

References

- [1] Roshko A. A new hodograph for free-streamline theory. NACA Technical Note No. 3168; 1954.
- [2] Lichtarowicz A, Markland E. Calculation of potential flow with separation in a right-angled elbow with unequal branches. *J Fluid Mech* 1963;17:596–606.
- [3] Mankbadi RR, Zaki SS. Computations of the contraction coefficient of unsymmetrical bends. *AIAA J* 1986;24:1285–9.
- [4] Chu SS. Separated flow in bends of arbitrary turning angles, using the hodograph method and Kirchhoff's free streamline theory. *J Fluids Eng* 2003;119:438–42.
- [5] Hassenpflug WC. Free-streamlines. *Comput Math Appl* 1998;36(1):69–129.
- [6] Hassenpflug WC. Branched channel free-streamlines. *Comput Methods Appl Mech Eng* 1998;159:329–54.
- [7] Monaghan JJ. Smoothed particle hydrodynamics. *Annu Rev Astron Astrophys* 1992;30:543–74.
- [8] Rosswog S. Astrophysical smooth particle hydrodynamics. *New Astron Rev* 2009;53:78–104.
- [9] Springel V. Smoothed particle hydrodynamics in astrophysics. *Annu Rev Astron Astrophys* 2010;48:391–430.
- [10] Libersky LD, Petschek AG, Carney TC, Allahdadi FA. High strain Lagrangian hydrodynamics: a three dimensional SPH code for dynamic material response. *J Comput Phys* 1993;109:67–C75.
- [11] Monaghan JJ. Simulating free surface flows with SPH. *J Comput Phys* 1994;110:399–406.
- [12] Liu MB, Liu GR. Smoothed particle hydrodynamics (SPH): an overview and recent developments. *Arch Comput Methods Eng* 2010;17:25–76.
- [13] Monaghan JJ. Smoothed particle hydrodynamics and its diverse applications. *Annu Rev Fluid Mech* 2012;44(1):323–46.
- [14] Price DJ. Smoothed particle hydrodynamics and magnetohydrodynamics. *J Comput Phys* 2012;231:759–94.
- [15] Lastiwka M, Basa M, Quinlan NJ. Permeable and non-reflecting boundary conditions in SPH. *Int J Numer Methods Fluids* 2009;61:709–24.
- [16] Hou Q, Zhang LX, Kruisbrink ACH, Tijsseling AS. Rapid filling of pipelines with the SPH particle method. *Procedia Eng* 2012;31:38–43.
- [17] Hou Q, Kruisbrink ACH, Tijsseling AS, Keramat A. Simulating transient pipe flow with corrective smoothed particle method. BHR group, 11th international conference on pressure surges, Lisbon, Portugal; 2012. p. 171–88.
- [18] Hou Q, Tijsseling AS, Bozkuz Z. Dynamic force on an elbow caused by a traveling liquid slug. *J Pressure Vessel Technol*, ASME, submitted for publication.
- [19] Reichl PJ, Morris P, Hourigan K, Thompson MC, Stoneman SAT. Smooth particle hydrodynamics simulation of surface coating. *Appl Math Model* 1998;22:1037–46.
- [20] Molteni D, Colagrossi A. A simple procedure to improve the pressure evaluation in hydrodynamic context using the SPH. *Comput Phys Commun* 2009;180:861–72.
- [21] Hou Q. Simulating unsteady conduit flows with smoothed particle hydrodynamics. PhD thesis, Eindhoven University of Technology, Eindhoven, The Netherlands; 2012. <<http://repository.tue.nl/733420>>.
- [22] Morris JP, Fox PJ, Zhu Y. Modelling low Reynolds number incompressible flows using SPH. *J Comput Phys* 1997(136):214–26.
- [23] Griebel M, Dornseifer T, Neunhoffer T. Numerical simulation in fluid dynamics: a practical introduction. Philadelphia: SIAM; 1998.
- [24] Marrone S, Antuono M, Colagrossi A, Colicchio G, Le Touzé D, Graziani G. δ -SPH model for simulating violent impact flows. *Comput Methods Appl Mech Eng* 2011;200:1526–42.
- [25] Adami S, Hu XY, Adams NA. A generalized wall boundary condition for smoothed particle hydrodynamics. *J Comput Phys* 2012;231:7057–75.
- [26] Cummins SJ, Rudman M. An SPH projection method. *J Comput Phys* 1999;152:584–607.

- [27] Liu X, Xu HH, Shao SD, Lin PZ. An improved incompressible SPH model for simulation of wave–structure interaction. *Comput Fluids* 2013;71:113–23.
- [28] Kruisbrink ACH, Pearce FR, Yue T, Cliffe A, Morvan H. SPH concepts for continuous wall and pressure boundaries. In: The 6th International SPHERIC workshop proceedings, Hamburg, Germany; 2011. p. 298–304.
- [29] Federico I, Marrone S, Colagrossi A, Aristodemo F, Veltri P. Simulating free-surface channel flows through SPH. In: 5th International SPHERIC workshop, Manchester, UK; 2010.
- [30] Shao SD, Lo EYM. Incompressible SPH method for simulating Newtonian and non-Newtonian flows with a free surface. *Adv Water Resour* 2003;26:787–800.
- [31] Fulk DA, Quinn DW. An analysis of 1-D smoothed particle hydrodynamics kernels. *J Comput Phys* 1996;126:165–80.
- [32] Monaghan JJ. Smoothed particle hydrodynamic simulations of shear flow. *Mon Not R Astron Soc* 2006;365:199–213.
- [33] Thomas PA, Couchman HMP. Simulating the formation of a cluster of galaxies. *Mon Not R Astron Soc* 1992;257:11–31.
- [34] Lee ES, Moulinec C, Xu R, Violeau D, Laurence D, Stansby P. Comparisons of weakly compressible and truly incompressible algorithms for the SPH mesh free particle method. *J Comput Phys* 2008;221:8417–36.
- [35] Couchman HMP, Thomas PA, Pearce FR. HYDRA: an adaptive–mesh implementation of PPPM–SPH. *Astrophys J* 1995;452:797–813.
- [36] Quinlan NJ, Lastiwka M. Truncation error in mesh-free particle methods. *Int J Numer Methods Eng* 2006;66:2064–85.
- [37] Vaughan GL, Healy TR, Bryan KR, Sneyd AD, Gorman RM. Completeness, conservation and error in SPH for fluids. *Int J Numer Methods Fluids* 2008;56:37–62.
- [38] Ellero M, Adams NA. SPH simulations of flow around a periodic array of cylinders confined in a channel. *Int J Numer Methods Eng* 2011;86:1027–40.
- [39] Peng W, Parker DF. An ideal fluid jet impinging on an uneven wall. *J Fluid Mech* 1997;333:231–55.
- [40] Antuono M, Colagrossi A, Marrone S, Molteni D. Free-surface flows solved by means of SPH schemes with numerical diffusive terms. *Comput Phys Commun* 2010;181:532–49.